

Short-lived Radio Bursts from the Crab Pulsar

J. H. Crossley¹, J. A. Eilek^{2,3}, T. H. Hankins^{2,3}, J. S. Kern¹

jeilek@aoc.nrao.edu

ABSTRACT

Our high-time-resolution observations reveal that individual main pulses from the Crab pulsar contain one or more short-lived microbursts. Both the energy and duration of bursts measured above 1 GHz can vary dramatically in less than a millisecond. These fluctuations are too rapid to be caused by propagation through turbulence in the Crab Nebula or the interstellar medium; they must be intrinsic to the radio emission process in the pulsar. The mean duration of a burst varies with frequency as ν^{-2} , significantly different from the broadening caused by interstellar scattering. We compare the properties of the bursts to some simple models of microstructure in the radio emission region.

Subject headings: pulsars: general; pulsars: individual (Crab pulsar)

1. Introduction

As part of the quest to understand how pulsars make coherent radio emission, we must understand how available energy in the pulsar’s magnetosphere is converted to radio emission. For instance, unshielded electric fields can drive relative streaming of electrons and positrons, either in outflows from the polar caps or in “gap” regions in the upper magnetosphere. The energy of these plasma streams is, in principle, available to be converted to radiation. Energy stored in disordered magnetic fields may also be available to be converted to radio emission. The relevant physical scales are probably large (tens of km or more, corresponding to millisecond timescales), and are manifested by pulsar mean profiles which reveal the radio-loud regions in the magnetosphere. On very small scales, this available energy is somehow converted to the collective charge motions which actually create the coherent radio emission. We expect this to take place on scales comparable to the plasma scale (typically tens of cm). An example of this may be the “nanoshots”, lasting no longer than a nanosecond, which Hankins et al. (2003) found in the main pulse of the Crab pulsar (also see Hankins & Eilek 2007). These nanoshots may reveal the fundamental emission process in

¹National Radio Astronomy Observatory, Socorro, NM 87801

²Physics Department, New Mexico Tech, Socorro, NM 87801

³Adjunct Astronomer, National Radio Astronomy Observatory

their region of origin; one likely model is soliton collapse in strong plasma turbulence (Weatherall 1998).

However, we do not yet understand how these two spatial scales are coupled. Just how are plasma dynamics on magnetospheric scales (hundreds of km) connected to the very small scales (tens of cm) involved in coherent radio emission? We suspect the answer will come from *microstructure*, which we define as significant pulse structure on ~ 1 to $100 \mu\text{s}$ timescales (corresponding to 0.3 to 30 km spatial scales).

1.1. Models of microstructure

Microstructure has been known to exist almost since pulsars were discovered (Craft et al. 1968, Hankins 1971). Although a variety of models have been proposed to explain the phenomenon, none has emerged as definitive.

Early models tended to be based on geometry. Various authors have proposed narrow, long-lived structures (flux tubes, say) which exist within the open field line region. These structures radiate by coherent curvature radiation as they rotate past the line of sight (e.g., Benford 1977; Lange et al. 1998). In this picture, the microsecond timescales reflect the size or beaming angle of the radio-loud structures. A variant of this model proposes localized charge clouds which intersect the line of sight only briefly as they move out along open field lines (e.g., Cordes 1981; Gil & Melikidze 2005). The timescales then reflect the time during which a given charge cloud beams its radiation into the observer’s line of sight.

Alternative models have also been proposed. Microstructure has been suggested to come from intrinsic temporal variability of the radio emission, possibly due to dynamic instabilities or unsteady flow in the emitting plasma (e.g., Sheckard, Eilek & Hankins 2010), for instance by magnetically driven flares (Lyutikov 2003). Timescales here would be those of the underlying instability (such as magnetic reconnection). Still another class of model identifies microstructure with propagation effects in the magnetosphere. Petrova (2004) proposes that microstructure is caused by the variable gain in stimulated Compton scattering; the timescale reflects the angular width of the high-gain radiation beam as it rotates past the line of sight. Cairns, Johnston & Das (2003) suggest microstructure comes from the stochastic growth of a signal passing through a turbulent plasma.

1.2. Goal of this work

To discriminate among these theories, we need observations that can confront the models. Traditionally microstructure has been treated statistically (e.g., Hankins 1972; Cordes, Weisberg & Hankins 1990; Lange et al. 1998), but such methods can obscure important details of the process.

We therefore turn to sensitive observations of individual pulses at sub-microsecond time resolution.

The Crab pulsar is an opportune target for single-pulse microstructure studies. Its occasional very bright pulses (by which it was discovered; Staelin & Reifenstein 1968) are good targets for our high-time-resolution data acquisition system (Hankins et al. 2003). At frequencies above ~ 1 GHz, single pulses from the Crab pulsar consist of one to several components, each lasting ~ 1 –100 microseconds. We call these *microbursts* (or simply *bursts*). In many pulses these bursts are sufficiently far apart in time that we can identify and characterize each one. Sallmen et al. (1999) show a few examples of single pulses at 1.4 GHz, taken from two of the data sets we analyze in this paper; Hankins & Eilek (2007) show a few examples observed at 9 GHz. As we show here, the properties of these bursts are highly variable. The number of bursts varies from one pulse to the next; the rotational phase, energy, and duration of a burst can vary between consecutive pulses and even within a single pulse.

In this paper we describe the microbursts we have detected in high-time-resolution, single-pulse observations of the main pulse of the Crab pulsar. We restrict ourselves to the main pulse for two reasons. First, pulses bright enough to be detected by our data acquisition system at frequencies below 5 GHz are much more common at the rotational phase of the main pulse than that of the interpulse (Cordes et al. 2004). We recorded some bright interpulses in a few VLA observing sessions at 1.4 and 4.8 GHz. Inspection of these data shows that these interpulses also contain microsecond-long bursts, very similar to those of the main pulse which we present in this paper. However, bright interpulses below 5 GHz are too rare in our data to constitute a statistically significant sample. In addition, the interpulse of the Crab pulsar seems to change its character, and its rotational phase, at high radio frequencies. The phase of the radio interpulse remains steady from 0.1 to 1.4 GHz, and is consistent with phase of the interpulse at optical and X-ray frequencies (Rankin et al. 1970; Moffett & Hankins 1996); but the interpulse seen between ~ 5 and 10 GHz occurs at a slightly earlier rotational phase (Moffett & Hankins 1996). Both the temporal and spectral characteristics of the interpulse between ~ 5 and 10 GHz are dramatically different from those of the main pulse at the same frequencies (Hankins & Eilek 2007). We therefore restrict ourselves here to the main pulse of the Crab pulsar.

Our high-time-resolution observations need the brightest pulses, which have been loosely called “giant” pulses in the literature. There has been discussion as to whether or not such bright pulses from the Crab pulsar are typical of the general pulse population (and thus, whether or not conclusions drawn on the basis of bright pulses can be applied to general pulsar emission physics). Lundgren et al. (1995) suggested that giant pulses at 0.6 GHz are a separate population from more typical, fainter pulses. Neither Popov & Stappers (2007) nor Sheckard et al. (2010) found any sign of a bimodal pulse distribution at 1.4 GHz, but Karuppusamy et al. (2010) find a possible second population at their fainter sensitivity limits. We do not pursue this question in this paper, but note that the pulses we study here correspond to the high-energy tail of bright-pulse distributions measured by these authors.

In the rest of this paper we present our data and characterize the microburst distribution of the main pulse of the Crab pulsar. In §2 we describe the observations; in §3 we describe the functional fitting we use to measure the bursts. In §4 we discuss the variability and energetics of the bursts. In §5 we discuss the durations of the bursts, and show that above ~ 1 GHz the burst widths are intrinsic to the star. We conclude with a short discussion in §6.

2. Observations

We recorded single pulses from the Crab pulsar in several observing sessions at the Very Large Array (VLA)¹ between 1993 (MJD 49080) and 1999 (MJD 51218). We used the VLA in phased-array mode, in which individual antenna delays are set in real-time so as to restore the original wave front. Even in the short-baseline, D-array configuration, the VLA at both 1.4 and 4.9 GHz synthesizes such a small angular beam that it is insensitive to most of the structure of larger angular size in the Crab Nebula when pointed at the pulsar. We therefore attained a much lower system temperature on the Crab pulsar than is possible with a single-dish telescope of equivalent collecting area.

The software package TEMPO (Taylor & Weisberg 1989) was used in prediction mode to create a pulsar timing model based on the monthly Crab pulsar ephemeris published by Jodrell Bank Observatory² (Lyne, Pritchard & Graham-Smith 1993). The timing model was used to set a period-synchronous gate at the pulse phase of the Crab main pulse. For each pulsar period the signal within the gate was square-law detected with a 200- μ s time constant. If the average flux of the pulse within this gate exceeded a preset multiple (typically 7) of the root-mean-square off-pulse noise, the pulse was recorded: the two orthogonal, circularly polarized signal voltages were digitally sampled by a LeCroy oscilloscope at a rate of 100 MHz. The samples were then transferred to disk for subsequent off-line coherent dedispersion (Hankins 1971). During the data transfer time, 10–30 s, the data acquisition was disabled, and no pulses could be captured.

In this paper we consider only those observing sessions in which no fewer than 27 strong main pulses were recorded. This number was chosen, after examining the data, to include a useful and interesting ensemble of observing sessions but to avoid observing sessions with statistically insignificant numbers of pulses.

This leaves us with 26 VLA observing sessions, listed in Table 1. Most of our observations were made between 1.2 and 1.7 GHz, or between 4.5 and 5.0 GHz; we include one observing session at 0.33 GHz. All observations were made with 50-MHz bandwidth, with two exceptions: the lowest frequency observations allowed only 3.125-MHz bandwidth at 0.33-GHz center frequency,

¹The Very Large Array is an instrument of the National Radio Astronomy Observatory, a facility of the National Science Foundation operated under cooperative agreement by Associated Universities, Inc.

²<http://www.jb.man.ac.uk/~simspulsar/crab.html>

and a simultaneous two-frequency observation at 1.2 and 1.7 GHz used 25-MHz bandwidth at each frequency. Table 1 also lists the number of pulses and microbursts fitted (as described in §3), the smoothing time used for the fits, the span of time between first and last recorded pulse, and the MJD for each observing session. In total, the VLA observations reported here include 1551 Crab pulses which contain 2969 fitted microbursts.

Seven of the observing sessions listed in Table 1 were simultaneous two-frequency observations, in which the VLA was split into two independent sub-arrays. Since interstellar dispersion causes the lower frequency signal to arrive later, we set the period-synchronous gate to monitor the pulse energy of the higher-frequency sub-array. If a pulse was recorded there, the oscilloscope was triggered again, after the appropriate digitally controlled dispersion delay, to record the pulse again in the lower frequency band. These seven pairs of observing sessions can be identified by the superscripts on the first column of Table 1; corresponding superscripts denote simultaneously recorded data.

We also used the same data acquisition system and observing procedure to record single pulses from the Crab pulsar in a few observing sessions at Arecibo Observatory³ in 2002. These are listed in Table 2. We did not carry out our full microburst analysis on these data sets, but we do use them in our statistical analysis of microburst widths, discussed in §5.

3. Microburst Function Fitting

Figure 1 shows several examples of individual pulses we recorded between 0.33 and 4.9 GHz. These examples are characteristic of the full data set. At all frequencies above 0.33 GHz single pulses contain one to several microbursts which are sufficiently well separated to be identified individually. The bursts can vary significantly in amplitude, duration, arrival phase, and total energy, from pulse to pulse and even within a given pulse.

3.1. Fitting function and procedure

To analyze the microbursts, we fitted analytic functions to individual bursts in each pulse. Inspection of our data showed that a fast-rise, slow-decay function, $F(t) \propto te^{-t/\tau}$ (as illustrated in Figure 1), is a good match to most of the individual bursts (as we discuss in §3.2). We therefore chose this as our fitting function. Our fitting procedure was as follows.

After coherent dedispersion (Hankins 1971), the off-pulse mean intensity, F_{off} , is calculated and subtracted from each individual pulse. We note that F_{off} consists of the receiver system temperature and a contribution from the Crab Nebula. We fit the remaining pulse flux as a sum of N component

³Arecibo Observatory is part of the National Astronomy and Ionosphere Center, which is operated by Cornell University under a cooperative agreement with the National Science Foundation.

bursts,

$$F(t) = \sum_{i=1}^N F_i(t; A_i, \tau_i, t_{0i}) \quad (1)$$

where the i^{th} burst is

$$F_i(t; A_i, \tau_i, t_{0i}) = A_i(t - t_{0i}) e^{-(t-t_{0i})/\tau_i}. \quad (2)$$

This function is illustrated in Figure 2, and examples of fitted microbursts are shown by dashed lines in each pulse of Figure 1. Each burst, F_i , is described by three parameters: its start time t_{0i} , its amplitude A_i , and its decay time τ_i . From these, we derive the burst’s maximum flux $F_{\text{max},i} = A_i\tau_i e^{-1}$, which occurs at its time-of-arrival, $t_{\text{TOA},i} = t_{0i} + \tau_i$. In what follows we measure the burst’s duration by its full width, $W_i = 3\tau_i$, which is approximately equal to the length of time that the flux exceeds $F_{\text{max},i}/e$. In the rest of this paper, we drop the “max” subscript and use “ F ” to denote the maximum flux of a burst.

The total energy of a burst is related to the time-integrated flux, which we call the *fluence*: $\mathcal{E} = \int F_i(t) dt = A_i\tau_i^2 = F_i W_i e/3$. To convert \mathcal{E} to total burst energy, E , we must know the distance to the pulsar, D ; the bandwidth of the radiation, $\Delta\nu$; and the angular width of the radiation beam, θ : $E = \mathcal{E}\Delta\nu D^2\theta^2$. We present most of our results here in terms of the fluence, \mathcal{E} , which is the directly measured quantity; we discuss the underlying energy release in §4.2 and §5.5, below.

We used up to six terms in our fits, ($1 \leq N \leq 6$), as needed for each pulse, so that uncertainties in the function parameters were small and the pulse residuals were close to being normally distributed about zero with standard deviation $\sigma(t)$, as given by the radiometer equation. For the on-pulse region, that standard deviation is

$$\sigma_{\text{on}}(t) = [F(t) + F_{\text{off}}]/\sqrt{\Delta\nu \Delta t} \quad (3)$$

while for the off-pulse region,

$$\sigma_{\text{off}} = F_{\text{off}}/\sqrt{\Delta\nu \Delta t} \quad (4)$$

where $\Delta\nu$ is the observing bandwidth and Δt is the smoothed time resolution.

For each pulse, the microbursts were initially identified by inspection, and the three parameters, A_i , t_{0i} , and τ_i , were carefully estimated by eye. We then used χ^2 minimization to obtain the best fit of $F(t)$ to the data. In computing χ^2 for a given set of parameters ($A_i, \tau_i, t_{0i}, i = 1, N$), every j ’th data sample must be assigned a standard deviation, σ_j , to represent its uncertainty. After experimenting with a variety of methods for calculating σ_j , we found that using the constant off-pulse standard deviation for all samples gives fits with the best residuals after χ^2 minimization. Using $\sigma_j = \sigma_{\text{on}}(t)$ as the standard deviation *unweights* the strongest parts of the pulse and χ^2 minimization yields poor fits. Thus, the standard deviation σ_j used to compute χ^2 is formally the same as the standard deviation, σ_{off} ; after χ^2 minimization we judge the fit according to $\sigma_{\text{on}}(t)$ to avoid non-physical χ^2 minima.

Although the fits were carried out using the full time resolution of the data (usually 10 ns), we smoothed and decimated the data before identifying the bursts, typically to 0.8 μs for pulses

below 2 GHz, and to $0.2 \mu\text{s}$ at higher frequencies. Table 1 gives the smoothing time used for each data set.

3.2. How robust are the microburst fits?

We find that the fast-rise, slow-decay function given in equation (2) fits the microbursts well at low frequencies. At our lowest frequency, 0.33 GHz, the single pulse profiles are very well fitted with a single $F(t)$ function (i.e., $N = 1$ in equation 1), as illustrated by pulse 1 in Figure 1. This agrees with previous results; Rankin et al. (1970) showed that the function in equation (2) is a good description of the pulsar’s mean profiles between 0.074 and 0.43 GHz.

At higher frequencies, however, the microburst shape begins to deviate from the fast-rise, slow-decay shape of our fitting function. Between 1.2 and 1.7 GHz, microbursts are still well matched to our fast-rise, slow-decay function, but they show occasional deviations from the functional form at the beginning or end of the microburst. For example, see pulse 6 in Figure 1. Above 4.5 GHz, the bursts show less of the slow-decay tail, and tend to be more symmetric about their peak than bursts at lower frequencies. In addition, higher-frequency bursts can contain very narrow bursts of emission superimposed upon broader features which may resemble the fast-rise, slow-decay shape of our fitting function. Examples can be found in pulses 9 and 10 in Figure 1.

Our fitting procedure clearly misses narrow and weak bursts. The narrowest burst we can identify is determined by our smoothing time, which is at least twenty times larger than our intrinsic time resolution. Because our fitting procedure is less than robust when bursts overlap in time, we can miss very narrow bursts which are superimposed on a broader burst of similar strength. We also clearly miss weaker bursts, for two reasons. First, we recorded only the stronger pulses, because we triggered our data acquisition system on the fluence of a pulse. In addition, weaker bursts in a multi-burst pulse might not be picked out by our fitting procedure.

3.3. Bursts seen simultaneously at two frequencies

We compared individual pulses in the data sets which were recorded simultaneously at two different frequencies (denoted by superscripts in Table 1). We determined by inspection that the same microburst can be identified at both the high and low frequency in some, but not all, frequency pairs. We can identify the same burst at two different frequencies if those two bands are both between 1 and 2 GHz, or both between 4 and 5 GHz. Examples of the same bursts which can be identified in pulses observed simultaneously at two frequencies are shown in pulse pairs 2 and 3, 4 and 5 or 10 and 11 of Figure 1.

However, we could not reliably identify individual bursts at both frequencies in pulses observed simultaneously at 1.4 and 4.9 GHz, as exemplified by pulses 7 and 8 in Figure 1. Thus, our fractional

microburst bandwidth, $\Delta\nu/\langle\nu\rangle$, is at least a factor $\sim 1/3$, but does not exceed unity. At first glance this seems to contradict the result reported by Moffett (1997), that 90% of bright pulses detected at 4.9 GHz were also detected at 1.4 GHz. Similarly, Sallmen et al. (1999) found that 70% of bright pulses detected at 1.4 GHz were also seen at 0.6 GHz. We conclude that although a bright pulse can be broadband (extending to an upper frequency at least 2-3 times the lower frequency), the microbursts which comprise it are relatively narrow-band. Whatever the physical process that releases energy into a bright pulse, it does so by means of a set of microbursts, each emitting in its own band of radio-frequencies.

4. Microburst variability and energy

Our basic measured quantities are the flux, F , and width, W , of an individual microburst. As example pulses in Figure 1 illustrate, both the flux and width of a burst can vary dramatically, on timescales as short as several microseconds, even within a single pulse.

To show this, we first present our results as (F, W) plots, grouped by observing frequency, in Figure 3. Each point is plotted with error bars denoting the fitting uncertainty in each quantity; nearly all of the points have uncertainties no larger than the plotting symbol used. (A very few data points, plotted as triangles, do not have error bars because the uncertainties are large enough to push the bounds of the error bars beyond the limits of one or both axes.) Despite the wide variation possible from burst to burst, Figure 3 shows that the distribution of individual bursts is localized in (F, W) space. As discussed above, in §3.2, our method misses weak and narrow overlapping pulses; the lower and leftmost boundaries of the (F, W) distributions are not physical. However, the lack of points in the upper right of each plot is physical; we would easily have detected such strong, wide bursts.

In this figure we have combined our data from different observing epochs into frequency groups. Although the flux and width can vary widely from burst to burst, we determined by inspection of individual data sets that the apparent “centroid” of the (F, W) distribution, at a given frequency, varies by no more than a factor of a few between observing sessions. Data from the individual epochs are presented in Crossley (2009). The small variation of mean fluxes we find agrees with previous authors (Rickett & Lyne, 1990, at 0.8 GHz, Lundgren et al., 1995, at 0.61 GHz, and Rankin et al., 1974, 0.073 to 0.43 GHz) who found the flux of time-averaged Crab pulses varied by only a factor of a few on timescales of several days to a few hundred days.

4.1. Fluence and energy range for bursts

It is well known that pulsar radio emission is highly variable from pulse to pulse, at least when observed at lower time resolution. Our results show that this variability also holds at the microburst level.

We overlay lines of constant fluence in each (F, W) plot in Figure 3. The fluence values of our bursts range over a factor ~ 100 ; we emphasize again that such variability can occur within a single pulse. The fluence range can also be seen in histograms of the burst fluence distribution, shown in Figure 4, again grouped by frequency. The apparent decay of the histograms below $\sim 10^{-2}$ Jy-s (1.2-1.7 GHz), or below $\sim 10^{-3}$ Jy-s (4.5-5.0 GHz) is not physical, but is due to incomplete sampling of weak pulses. The fluence at which the histograms peak corresponds approximately to the threshold we used to record a single pulse (discussed in §2). The high-fluence side of the histograms is physical, however, reflecting the true distribution of burst fluence above our trigger threshold.

The steepening of the burst fluence distribution at high fluence values is also consistent with previous statistical studies of single pulses from the Crab pulsar. Several authors (Moffett 1997, Popov & Stappers 2007, Bhat et al. 2008, Sheckard et al. 2010, Karuppusamy et al. 2010) used observations at lower time resolution to characterize the fluence distribution of total pulses (not separated into microbursts). While details of the methods differ, all seem to agree that the total pulse fluence distribution at 1.4 GHz steepens around $\sim 3 - 10 \times 10^{-3}$ Jy-s. Thus, at the higher fluence values which our trigger threshold allowed us to sample, there is evidence that the fluence distribution is not a simple power law, but is in fact a convex function, steepening towards higher fluence. Although we are measuring burst fluence, not total pulse fluence, most pulses contain no more than one very strong burst. The high-fluence shape of our burst distribution therefore appears to be consistent with these previous studies.

Figure 3 also shows a tendency for brighter bursts to be shorter-lived, and for weaker bursts to be longer-lived. This is consistent with previous results on single pulses (not bursts) seen at lower time resolution. Bhat et al. (2008) compared the strength of a pulse to its effective width, defined in a matched-filtering sense; Karuppusamy et al. (2010) compared the strength of a pulse to its equivalent width. Both papers found that brighter pulses tend to be shorter-lived.

To connect our observations to the range of energies released in a burst, we must convert the observed fluence to energy. As discussed in §3.1, the energy of a burst is related to its fluence by $E = \mathcal{E} \Delta\nu D^2 \theta^2$. We know the distance to the pulsar ($D = 2$ kpc); from our simultaneous two-frequency observations (§3.3) we can estimate $\Delta\nu \sim 0.5\nu$. Our typical burst fluence at 1.4 GHz is $\mathcal{E} \sim 10^{-2}$ Jy-s, and a factor ~ 10 lower at 5 GHz, but burst fluences can vary by a factor ~ 10 up or down from these values. To convert to energy, we guess that a burst is beamed into an angle $\theta \sim 1/\gamma$, where γ is the Lorentz factor of the emitting plasma. This puts the energy released at the star at $\sim (10^{26} - 10^{28})/\gamma^2$ erg in the bursts we detected at 1.4 GHz. In addition, it is very likely that many weaker bursts exist below our detection threshold.

4.2. What can we learn from microburst strengths?

We are not aware of many models which can be compared to our observed burst energies; the nonlinear physics involved in coherent radio emission make such predictions challenging. One attractive idea which can be tested is the suggestion that bursts represent an energy storage and release mechanism, so that all bursts would release the same energy at the star (e.g., Benford 2003). The distribution of points in Figure 3 is suggestive of an energy-conserving relationship; stronger bursts tend to be shorter-lived, and weaker bursts tend to be longer-lived. However, the situation is not so simple, because observed bursts occupy a range ~ 100 in fluence, which seems to suggest a wide range in burst energy. Nonetheless, it may be that the bursts all have the same energy in the rest frame of the emitting plasma, and that their observed fluence range is due to relativistic beaming. We explore two simple versions of this idea.

One possibility is that the Lorentz factor of the emitting plasma is constant for all bursts, but the angle between the plasma motion and the line of sight, θ , varies burst to burst. This is easy to test. If E_0 is the burst energy measured in the plasma rest frame, we observe energy $E = E_0/\gamma(1 - \beta\mu)$, for $\mu = \cos\theta$. If the bursts are emitted isotropically in the plasma rest frame, we will observe a burst energy distribution, $n(E) \propto d\mu/dE \propto 1/E^2$. Because $\mathcal{E} \propto E$ in this scenario, we should see a fluence distribution, $n(\mathcal{E}) \propto 1/\mathcal{E}^2$. We illustrate this prediction with a dashed line in the fluence histograms of Figure 4. For well-sampled frequencies (1.2 to 5 GHz), the figures show that a small range of the high- \mathcal{E} distribution does appear consistent with the $1/\mathcal{E}^2$ prediction. However, for stronger bursts the distribution drops more rapidly than $1/\mathcal{E}^2$. We thus conclude that this hypothesis fails: microbursts are not all emitted with the same energy from plasma moving at a single Lorentz factor.

Alternatively, the observed fluence range may be caused by the Lorentz factor, γ , varying from burst to burst. For angles within the beaming cone, $\theta \lesssim 1/\gamma$, the factor $1 - \beta\mu \simeq 1/2\gamma^2$. The observed burst energy becomes $E \sim 2\gamma E_0$, and the observed fluence becomes $\mathcal{E} \sim 2\gamma^3 E_0$. (This strong dependence on γ reflects the change in the beaming angle as well as the simple Doppler boost of the burst energy). Thus, a small variation in γ , by a factor $\lesssim 5$, can lead to the observed factor ~ 100 variation in fluence that we observe. If such fluctuations do exist in the radio-loud region, then the energy-storage-and-release picture may be correct, and the $n(\mathcal{E})$ distribution reflects the underlying (and unknown) $n(\gamma)$ distribution. Because current models of the radio-loud region generally invoke steady flow in the emitting plasma, we cannot identify a simple model prediction to test against our data. However, given the dramatic fluctuations we see in the strength of the radio emission, we see no reason to assume steady flow; turbulent, unsteady flow with the necessary amplitude may well exist in the radio-loud region.

4.3. Strength of bursts seen at two frequencies

Figures 3 and 4 show that microbursts tend to be weaker at higher frequencies. This can be seen from the upper envelope of the (F, W) plots, which decreases from ~ 0.3 Jy-s at 0.33 GHz to ~ 0.03 Jy-s at 4.8 GHz. This trend is generally consistent with the steep spectrum of the Crab pulsar’s mean profile (e.g., Lorimer et al. 1995), but hard to specify due to incomplete sampling at lower fluence.

We can, however, be more quantitative if we restrict ourselves to individual microbursts identified at both frequencies in pulses simultaneously sampled at two frequencies. From these data sets we extract a total of 192 microbursts, which we can use to explore how the fluence of an individual microburst depends on frequency. Figure 5 compares the fluence of each burst at the two observed frequencies. Clearly the burst fluences are well correlated at the two frequencies. The bursts are usually weaker at the higher frequency, and show an approximately linear relationship between the fluence at the higher and lower frequency. The scatter in the figure is real, and substantially larger than errors from our fitting procedure.

We quantify the fluence-frequency correlation by measuring the spectral index, α , for each burst, defined as $\mathcal{E}(\nu) \propto \nu^\alpha$. Table 3 shows our results, expressed as the mean $\langle \alpha \rangle$ and its standard deviation, σ_α . Thus, our data suggest $\langle \alpha \rangle \sim -2$ for these microbursts, but with significant uncertainty. The relatively large scatter in the $\mathcal{E}(\nu_2)/\mathcal{E}(\nu_1)$ ratio for the set of bursts translates to the large uncertainty in the derived spectral indices (especially at the very small frequency separation between 4.5 and 4.9 GHz). It should be noted that our observing method introduces a bias for stronger pulses at higher frequency, because the fluence threshold used to record individual pulses is compared only with the higher frequency pulse, which arrives first at our detector. Our results are consistent with those of Moffett (1997), who measured a distribution of single pulse spectral indices between 1.4 and 4.9 GHz which peaked in the range $-2.0 < \alpha < -1.5$.

5. Microburst duration

Microbursts vary significantly in duration (width), even within a single observing epoch at a single frequency. Some are shorter-lived (narrow), others are longer-lived (broad). Unlike the situation with burst energies, models do exist for the temporal structure of pulsed emission. At low frequencies, the observed pulse width is commonly thought to be caused by interstellar scattering (ISS). At higher frequencies, where ISS effects are small, microstructure models (as in §1.1) attempt to connect temporal variability to conditions in the pulsar’s magnetosphere. Our data allow us to verify the former idea, learn at what frequencies intrinsic broadening dominates ISS for the Crab pulsar, and establish properties of burst widths which future models must address.

5.1. Low frequencies: pulse broadening by ISS

At low frequencies, pulse widths — and by extension microburst widths — have generally been ascribed to ISS caused by turbulence in the Crab Nebula or the interstellar medium (ISM). In particular, several authors have studied pulse profiles of the Crab pulsar at frequencies below 1 GHz, either as mean profiles or single pulses. These authors find that pulses at these frequencies are broad, single bursts, with a consistent width and shape pulse to pulse, as would be expected from ISS. Our results at 0.33 GHz agree with this trend. We find only one burst per pulse, with little variation of burst width about the $\sim 600 \mu\text{s}$ mean.

In Table 4 we combine our results at 0.33 GHz with results from the literature; we show these results as open circles in Figure 6. Results in the literature are typically quoted in terms of the exponential decay time τ (related to our widths by $\tau = W/3$). We also overlay a $\tau(\nu) \propto \nu^{-4}$ line in Figure 6, to illustrate the width behavior predicted if the turbulence causing the ISS has a Gaussian spectrum. We note that small variations in the exponent of the $\tau(\nu)$ behavior have also been suggested. If the turbulence has a Kolmogorov spectrum, models predict $\tau(\nu) \propto \nu^{-4.4}$ (Lee & Jokipii, 1975). Kuzmin et al. (2002) fit $\tau(\nu) \propto \nu^{-3.8}$ to data between 0.04–2.23 GHz.

Figure 6 shows that the data below ~ 1 GHz are generally consistent with the ν^{-4} prediction (or possibly with one of its variants). The pulse widths below 1 GHz do show some scatter about the predicted ν^{-4} line. Some of this may be introduced by the fact that these measurements, taken from the literature, are not contemporaneous. The mean-profile pulse width of the Crab pulsar is known to vary on timescales of weeks or months; this is believed to be due to “weather” in the Crab Nebula (e.g., Isaacman & Rankin 1977). Extreme examples are the strong scattering events reported by Lyne & Thorne (1975), or Backer, Wong & Valanju (2000). To our knowledge the data in Table 4 were not obtained during such extreme events, but some secular variation may still be expected.

5.2. High frequencies: burst widths are intrinsic

Taken altogether, the data discussed in §5.1 support the idea that pulses seen below ~ 1 GHz are broadened by turbulence in the Crab Nebula and the ISM. At higher frequencies, however, the situation is very different.

Just as the energies of microbursts seen above ~ 1 GHz can vary over more than an order of magnitude within one pulse, on time scales $\sim 10\text{--}100\mu\text{s}$, so can their durations. This can be seen by inspection of the example pulses above ~ 1 GHz in Figure 1, which show that bursts within a single pulse can have vastly different widths. Both narrow and broad bursts can coexist and overlap in the same pulse. The burst widths we measured range over nearly two orders of magnitude. This is apparent in Figure 3, and also in Figure 7, which shows histograms of the burst widths, $n(W)$.

Microbursts seen above ~ 1 GHz are almost always longer-lived than the duration predicted

by ISS. Taking $600 \mu\text{s}$ as a typical width at 0.33 GHz, and extrapolating as $W(\nu) \propto \nu^{-4}$, we would expect widths determined by ISS to be $\sim 1 \mu\text{s}$ at 1.4 GHz. For comparison, the distribution of our measured widths peaks at $\sim 10 \mu\text{s}$. At 4.8 GHz, the distribution of our measured widths peaks at $\sim 1 \mu\text{s}$; but we would expect widths due to ISS to be only $\sim 10 \text{ ns}$. Once in awhile, however, the Crab pulsar emits very narrow nanoshots which are sparse enough in time to be detected individually. Hankins et al. (2003) detected a few nanoshots at 5 GHz which were unresolved with 2 ns instrumental resolution. Hankins & Eilek (2007) detected a nanoshot at 9 GHz which was unresolved at 0.4 ns resolution. We include these two results as open triangles in Figure 6, and note they fall approximately on the ν^{-4} ISS line. The duration of these nanoshots is consistent with the high-frequency extrapolation of ISS. Thus, individual nanoshots are sufficiently short-lived that they are subject to pulse broadening by ISS. However, the duration of the “clumps” of overlapping nanoshots which comprise most microbursts is too long to be due to ISS.

5.3. High frequencies: is nebular scattering important?

Because bursts seen above $\sim 1 \text{ GHz}$ last longer than predicted by ISS, and because their widths can vary in less than a millisecond, we suspect their durations are intrinsic to the pulsar. Other authors (Cordes & Lazio 2001, Karuppusamy et al. 2010) have disagreed, suggesting that scattering by structures in the Crab Nebula can account for pulse or burst widths even at high frequencies. We have, in fact, seen two likely examples of nebular scattering. On two observing days we saw strong, narrow bursts which were consistently followed by broad, weak bursts. We identified the weak bursts as “echoes” of the strong “primary” bursts (Crossley et al. 2007). In each case the echoes persisted for $10^4 - 10^5$ stellar rotations, at a steady $\sim 50 - 100 \mu\text{s}$ time lag and steady $\sim 1/3$ fluence ratio relative to the primary bursts. We suggested in Crossley et al. (2007) that these echoes may be caused by structures in the Crab Nebula which happen to cross the sightline to the pulsar.

Our two echo observations were unusual, however. Most of the microbursts we recorded seem to occur randomly in duration, rotation phase and amplitude. In particular, burst widths can vary dramatically within one stellar rotation, and sometimes within a single pulse. To explain this by nebular scattering, different scattering clouds must cross our sightline every few milliseconds. Such clouds must be very small, no larger than $L_{cl} \sim 300 \text{ km}$. Turbulent broadening from clouds this small almost certainly occurs in the confined-screen limit of Cordes & Lazio (2001). In this limit, the duration of the scattered burst is limited by the spatial extent of the cloud, not the turbulence level within the cloud. For a cloud at distance D_{cl} from the pulsar, the scattering width $\tau_{sc} \sim L_{cl}^2/2cD_{cl}$. To compare the predicted τ_{sc} to our observed widths, we must know D_{cl} . If the scattering cloud is associated with the Crab nebula, rather than the pulsar, it must be at or beyond the termination shock of the pulsar wind. Momentum balance says this shock should occur at $\sim 0.1 \text{ pc}$, which coincides nicely with the location of the quasi-stationary X-ray “ring” believed to be associated with that shock (e.g., Hester 2008). But now, the scattering width caused by a cloud 300 km in size, sitting at $D_{cl} \sim 0.1 \text{ pc}$, is only $t_{sc} \sim 10^{-14} \text{ s}$. Clearly this simple model cannot

explain the burst durations we observe.

Alternatively, to broaden a narrow burst to $\sim 10\mu\text{s}$, a 300-km cloud must be located at $D_{cl} \sim 10^4$ km from the pulsar. This distance is about 10 times the light cylinder radius, but well inside of the termination shock; thus the cloud is within the pulsar wind. Such small structures may exist in a pulsar wind, but their properties (size, magnetization, plasma content) are not well enough understood to explore this idea any further.

The nebular-scattering model is also called into question by the lack of clear evidence for turbulent scattering in burst profiles above ~ 4 GHz. Turbulent scattering creates an exponential tail on the scattered burst; but the bursts we recorded at 4–5 GHz tend to have a symmetric profile (as discussed in §3.2). The same is true for microbursts Hankins & Eilek (2007) detected in the main pulse between 6 and 10 GHz. It therefore seems likely that burst profiles above ~ 4 GHz reflect the temporal behavior of the fundamental energy-release process. On the other hand, bursts we recorded between 1–2 GHz do have a fast-rise, slow-decay shape. Their profile may be determined solely by the energy-release process, if that process has a different temporal signature than those which create higher-frequency bursts. The burst profile at 1–2 GHz may also be modified by scattering; if that is the case, our arguments above suggest that the scattering must happen no further from the pulsar than within its wind. Overall, it seems simplest to argue that all burst durations above ~ 1 GHz are intrinsic to the pulsar.

5.4. Frequency dependence of burst widths

Despite the wide range of burst durations we observed, figures 3 and 7 show that the “typical” width of a burst depends on frequency. Microbursts seen at higher frequency tend to be shorter-lived than those seen at lower frequency. We can quantify this using bursts observed simultaneously at two frequencies, as well as with statistical measures of our full data sets.

5.4.1. Individual bursts seen at two frequencies

As with burst energies, we can use simultaneous two-frequency observations to explore the frequency dependence of burst duration. Figure 8 compares the width of each burst at the two observed frequencies. We find that burst widths at the two frequencies are well correlated, but not identical. Lower frequency microbursts are typically longer-lived than their higher frequency counterparts, but again we find strong scatter about the correlation. As with the energy-energy correlations, the scatter in width-width correlations is real, and substantially larger than the errors in our fitting procedure. We quantify the width-frequency correlation by assuming the width obeys $W(\nu) \propto \nu^\beta$, where β is the width index. Table 3 shows our results, expressed as the mean $\langle\beta\rangle$ and its standard deviation, σ_β . Our data suggest $\langle\beta\rangle \sim -2$, again with significant uncertainty (as shown in the σ_β values).

5.4.2. Statistical measures of burst widths

We can also use our full set of measured bursts to investigate the $W(\nu)$ relation. We first simply estimate the mean width, $\langle W \rangle$, described by the $n(W)$ distributions in Figure 7. Because the width at which these histograms peak is not an artifact of our observation or analysis methods, but is intrinsic to the star, it is an accurate characterization of microburst durations. At 0.33 GHz, we estimate $\langle W \rangle \sim 600 \mu\text{s}$; $\sim 10 \mu\text{s}$ at 1.4 GHz; $\sim 5 \mu\text{s}$ at 1.7 GHz; and $\langle W \rangle \sim 1 \mu\text{s}$ at 4.8 GHz. These results are included as filled squares in Figure 6, where we again convert to decay times: $\langle \tau \rangle \sim 200 \mu\text{s}$ at 0.33 GHz; $\sim 3 \mu\text{s}$ at 1.4 GHz; $\sim 1.7 \mu\text{s}$ at 1.7 GHz; and $\langle \tau \rangle \sim 0.3 \mu\text{s}$ at 4.8 GHz.

For an alternative analysis, we might want to determine a mean burst width from each of our data sets. Because of the intrinsic jitter of the microbursts in pulse phase, we cannot simply average a set of pulses. That would give a mean pulse profile (or a form of the probability density function of microbursts in pulse phase) but not a mean burst profile. Instead, we work in the Fourier domain, where delays in arrival time are only phase shifts. When the modulus of the Fourier components is computed, the phase shifts are irrelevant. We therefore evaluate the mean fluctuation power spectrum of each set of pulses.

Our method is as follows. For each pulse in a data set, we use a Fast Fourier Transform to evaluate the fluctuation power spectra for both an on-pulse and an off-pulse region, letting f be the conjugate Fourier variable to time t . In the off-pulse region, multiple transforms are averaged to decrease the estimation error. The on-pulse spectrum is divided by the off-pulse spectrum to remove any (non-white) residual spectrum from the receiver bandpass. All of the corrected on-pulse spectra for a given observing session are normalized (to prevent a single strong pulse from dominating the result) and averaged (to derive a mean fluctuation spectrum).

In order to determine the characteristic timescale of the bursts, we fit an analytic function to the discretized mean fluctuation spectrum. We chose a generalized burst shape in the time domain,

$$G_n(t) = t^n e^{-t/\tau} \quad (5)$$

If $n + 1 > 0$, $G_n(t)$ has an analytic Fourier transform, $g_n(f)$; its squared amplitude is

$$|g_n(f)|^2 = \frac{\Gamma^2(n + 1)}{(4\pi^2 f^2 + 1/\tau^2)^{n+1}} \quad (6)$$

where $\Gamma^2(n + 1) = (n!)^2$ is the square of the usual Gamma function. We compared equation (6) to the mean fluctuation spectrum of 11 data sets, recorded at the VLA (picked from the Table 1), and at Arecibo (from Table 2), chosen to sample our frequency range well. We kept n as a fixed parameter, and used least-squares methods to determine the value of τ for each data set.

Although the $g_1(f)$ case recovers the function we used to fit individual bursts (equation 2), we found that this case does not fit any of our mean fluctuation spectra well. This is perhaps surprising, because our fitting function is well matched to the shape of individual microbursts, especially below 2 GHz. Nonetheless, we found that mean fluctuation spectra below 1.7 GHz are well fit by the

simpler $g_0(f)$ function, which is the transform of a one-sided exponential decay. Figure 9 shows an example of our fit to a fluctuation spectrum at 1.4 GHz. However, fluctuation spectra above 1.7 GHz were not well fit by $g_0(f)$ or $g_1(f)$. After experimentation we found that $g_{-1/2}(f)$ provides a better description of the mean fluctuation spectra at the higher frequencies. Figure 10 shows an example of this fit at 5.5 GHz, and also illustrates how poorly $g_0(f)$ matches these data. Because the corresponding time-domain function, $G_{-1/2}(t)$, diverges as $t \rightarrow 0$, we do not claim it is a true description of a “characteristic” microburst at all times. We suspect this apparently unphysical result comes from combining normalized fluctuation spectra of broad and narrow microbursts into one mean spectrum. We simply note that $g_{-1/2}(f)$ is a good representation of the data for our mean fluctuation spectra above 2 GHz, and use this representation to estimate the mean decay constants for those data sets.

Our results are summarized in Table 5, and included as asterisks in Figure 6. We were pleased to find that these mean decay constants are comparable to the simple estimates of burst duration which we made from the $n(W)$ histograms in Figure 7, even though they were derived by quite different methods. Both of these methods also agree with the width behavior we inferred from individual bursts seen at two frequencies. We conclude that the typical widths of microbursts seen above ~ 1 GHz obey $W(\nu) \propto \nu^{-2}$, but that significant burst-to-burst scatter also exists about this trend.

5.5. What can we learn from microburst widths?

We argued in the previous section that the duration of each microburst seen above ~ 1 GHz is set when it leaves the pulsar. The burst width must be caused either by the emission process, or by propagation through the star’s magnetosphere, or both. If this is the case, then our results provide simple constraints on different microstructure models, as follows.

One model holds that microbursts are due to long-lived geometrical structures or narrow radiation beams within the magnetosphere, (as discussed in §1.1). If the bursts are due to narrow flux tubes, radiating within an angle $\sim 1/\gamma$ as they rotate through the line of sight, their duration is $\sim P/2\pi\gamma$, where P is the pulsar’s rotation period. Thus, a range ~ 100 in observed burst duration requires that a range ~ 100 in the plasma Lorentz factor coexists between different flux tubes within the open field line region. Such large variation is not predicted by current models of plasma in the open field line region. Alternatively, if the bursts are due to small charge clouds moving out along a magnetic field line with curvature radius ρ , their duration is $\sim \rho/\gamma^3 c$. The observed range ~ 100 in burst duration requires a range $\lesssim 5$ in the Lorentz factor of different clouds observed within a single pulse. We argued above, in §4.2, that velocity fluctuations of this magnitude may not be unreasonable in a turbulent, radio-loud region.

Another type of model attributes microstructure to stimulated Compton scattering, and the sweep of a narrow, exponentially-enhanced radiation beam past the line of sight (e.g., Petrova

2004). These models are attractive, in that they have the potential to create widely varying pulse widths and energies, due to the extreme sensitivity of the exponential gain factor to local plasma parameters. Unfortunately, it is hard to derive simple, testable predictions from these models, due both to their complexity, and to the intrinsic nonlinear behavior of the underlying physics.

A third type of model argues that microstructure reflects intrinsic temporal variability of the underlying plasma. One example here is the hypothesis that bursts each release a constant energy, E_0 , as measured in the plasma rest frame (§4.2). Doppler beaming causes the fluence of such a burst to be $\mathcal{E} \propto \gamma^3 E_0$. If the bursts also have a constant rest-frame duration, τ_0 , relativistic and light travel effects shorten their duration as seen at earth to $\tau \sim \tau_0/\gamma$. Thus, the flux of the burst should obey $F \propto \mathcal{E}/\tau \propto \tau^4$. We see no such correlation in Figure 3. We conclude that, while constant-energy bursts with variable Lorentz factors can explain the range of fluences we see, the intrinsic duration of such bursts cannot also be constant.

A variant of this model suggests that the burst energy, E_0 , is released by a reconnection event, of scale L_0 and local magnetic field B , in a region of turbulent plasma. The duration of the event, as seen in the plasma rest frame, is $\sim L_0/c$ (noting that the reconnection flow speed is close to lightspeed in the relativistic plasma of the magnetosphere; Lyutikov 2003). Light-travel effects shorten its duration as seen at earth to $\tau \sim L_0/\gamma^2 c$. The few- μs pulse widths we see at 1.4 GHz therefore come from a region $L_0 \sim \gamma^2$ km. Because such a region must be smaller than the size of the magnetosphere, this picture can work only if the radio-loud plasma is moving fairly slowly ($\gamma \lesssim 10$, say). We expect the energy released in a reconnection event to be $E_0 \propto B^2 L_0^3$, leading to a fluence $\mathcal{E} \propto \gamma^2 B^2 L_0^3$ as seen at earth. A spread in L_0 can cause the observed spread in \mathcal{E} . If the pre-reconnection field B is roughly constant for each burst, the flux should obey $F \propto \mathcal{E}/\tau \propto \tau^2$. Once again, we see no such correlation in Figure 3. We conclude that this model can explain the data only if the pre-reconnection magnetic field tends to be weaker in larger (longer-lived) events.

6. Summary and Discussion

Our high-time-resolution observations reveal a wealth of structure within single pulses from the main pulse of the Crab pulsar, against which current and future models of pulsar radio emission and microstructure should be tested.

At 0.3 GHz, the pulse profile is smeared and broadened by ISS, which preserves the total pulse energy but broadens and distorts the profile into a fast-rise, slow-decay shape. We therefore cannot determine the intrinsic structure of a low-frequency pulse when it left the star. Above ~ 1 GHz, however, ISS effects become negligible, and the intrinsic pulse structure is revealed. We find that individual pulses contain one to several microbursts, each burst lasting on the order of microseconds. The bursts are often sparse enough and bright enough to be measured individually. We measured the duration, peak flux, and fluence of nearly 3000 bursts, at frequencies between 1.2 and 4.8 GHz, recorded in different observing sessions over several years.

Microbursts have only a modest bandwidth. When we carried out simultaneous, two-frequency observations, we found that individual bursts within a single pulse can be identified between 1.2 and 1.7 GHz, but not between 1.4 and 4.9 GHz. Thus, while a particular bright pulse can be broadband (detected over a factor $\gtrsim 2-3$ in frequency), the bursts it contains are relatively narrowband ($\Delta\nu/\langle\nu\rangle < 1$).

Microbursts at a given frequency can be bright or faint. There is some tendency for high-flux bursts to be shorter-lived and low-flux bursts to be longer-lived. Although this trend could suggest that all bursts release the same amount of energy, our measured burst fluences varied over more than a factor ~ 100 , and even weaker bursts are very likely common but below our detection threshold. It may be that this spread is caused by relativistic beaming of constant-energy bursts from a turbulent plasma in the radio-loud region. Unfortunately, models of the radio emission region are not yet developed to the point where specific tests against the data are possible.

Microbursts at a given frequency can be short or long, but they also tend to be briefer at higher frequency. Simultaneous two-frequency observations as well as statistical estimates from our full data sets suggest that the burst width becomes shorter with frequency approximately as $W(\nu) \sim \nu^{-2}$. Because bursts above ~ 4 GHz do not show the exponential tail characteristic of turbulent scattering, and because burst widths above ~ 1 GHz fluctuate on very short timescales, we argue that the burst duration is intrinsic to the energy release mechanism. The large range of burst durations may be caused, at least in part, by relativistic boosting from turbulent plasma in the radio emission region. However, current models of microstructure are not developed to the point where they can be quantitatively tested against the data.

We thank the technical, operations, and computer staffs at the Very Large Array and the Arecibo Observatory for their help with the data acquisition equipment, observing, and for providing the computing environment we used for the observations. We also thank David Moffett, Tracey Delaney and Joe Dickerson for help with the VLA observations. We are grateful to Jim Sheckard for many enlightening discussions of microstructure models, to Jim Weatherall for suggesting the relativistic beaming angle modification of a constant-energy burst, and to Jim Cordes for conversations about possible causes of pulse broadening. We thank the referee for perceptive suggestions which improved the paper. This work was partly supported by NSF grants AST-9618408, AST-0139641, and AST-0607492.

REFERENCES

- Backer, D. C., Wong, T. & Valanju, J. 2000, *ApJ*, 543, 740
Benford, G. 1977, *MNRAS*, 179, 311
Benford, G. 2003, *Phys Lett A*, 318, 412
Bhat, N. D. R., Tingay, S. J. & Knight, H. S. 2008, *ApJ*, 676, 1200

- Cairns, I. H., Johnston, S. & Das, P. 2003, MNRAS, 343, 512
- Cordes, J. M. 1981, in Proc of IAU Symposium 95: Pulsars, eds. R. Wielebinski & W. Seiber, 115
- Cordes, J. M., Weisberg, J. M. & Hankins, T. H. 1990, AJ, 100, 1882
- Cordes, J. M. & Lazio, T. J. W., 2001, ApJ, 549, 997
- Cordes, J. M., Bhat, N. D. R., Hankins, T. H., McLaughlin, M. A., Kern, J. 2004, ApJ, 612, 375
- Craft, H. D., Jr., Comella, J. M., Drake, F. D. 1968, Nature, 218, 1122
- Crossley, J. H., Eilek, J. A. & Hankins, T. H., 2007, in ASP Conference Series 365: SINS - Small Ionized and Neutral Structures in the Diffuse Interstellar Medium, ed. M. Haverkorn & W. M. Goss, 271
- Crossley, J. H. 2009, M.S. thesis, New Mexico Tech
- Gil, J. & Melikidze, G. I. 2005, A&A, 432, L61
- Hankins, T. H. 1971, ApJ, 169, 487
- Hankins, T. H. 1972, ApJ, 177, L11
- Hankins, T. H. & Eilek, J. A. 2007, ApJ, 670, 693
- Hankins, T. H., Kern, J. S., Weatherall, J. C., & Eilek, J. A. 2003, Nature, 422, 141
- Hester, J. H., 2008, ARA&A, 46, 127
- Isaacman, R. & Rankin, J. M., 1977, ApJ, 214, 214.
- Karuppusamy, R., Stappers, B. W. & van Straten, W., 2010, A&A, 515, A36
- Kuzmin, A. D., Kondrat'ev, V. I., Kostyuk, S. V., Losovsky, B. Ya, Popov, M. V., Soglasanov, V. A., D'Amico, N. & Montebugnoli, S. 2002, AstLett, 28, 251
- Lange, Ch., Kramer, M., Wielebinski, R. & Jessner, A. 1998, A&A, 332, 111
- Lee, L.C. & Jokipii, R. 1975, ApJ, 201, 532.
- Lorimer, D. R., Yates, J. A., Lyne, A. G. & Gould, D. M. 1995, MNRAS, 263, 411
- Lundgren, S. C., Cordes, J. M., Ulmer, M., Matz, S. M., Lumatch, S., Foster, R. S. & Hankins, T. H. 1995, ApJ, 453, 433
- Lyne, A. G., Pritchard, & Graham-Smith, F. 1993, MNRAS, 265, 1003
- Lyne, A. G. & Thorne, D. J. 1975, MNRAS, 172, 97
- Lyutikov, M. 2003, MNRAS, 346, 540
- Moffett, D. A. 1997, Ph.D. thesis, New Mexico Tech
- Moffett, D. A., & Hankins, T. H. 1996, ApJ, 468, 779
- Petrova, S. A. 2004, A&A, 424, 227
- Popov, M. V. & Stappers, B. 2007, A&A, 470, 1003

- Popov, M. V., Kuzmin, A. D., Ul'yanov, O. M., Deshpande, A. A., Ershov, A. A., Zakharenko, V. V., Kondratiev, V. I., Kostyuk, S. V., Losovskii, B. Ya & Soglasnov, V.A., 2006, *AstRep*, 50, 562
- Rankin, J. M., Comella, J. M., Craft, H. D. Jr., Richards, D. W., Campbell, D. B., & Counselman, C. C., III 1970, *ApJ*, 162, 707
- Rankin, J. M., Payne, R. R., & Campbell, D. B. 1974, *ApJ*, 193, L71
- Rickett, B. J. & Lyne, A. G. 1990, *MNRAS*, 244, 68
- Sallmen, S., Backer, D., Hankins, T., Moffett, D., & Lundgren, S. 1999, *ApJ*, 517, 460
- Sheckard, J., Eilek, J. A. & Hankins, T. H. 2010, in preparation.
- Staelin, D. H. & Sutton, J. M. 1970, *Nature*, 226, 69
- Staelin, D. H. & Reifenstein, E. C. III 1968, *Science*, 162, 1481
- Taylor, J. H., & Weisberg, J. M. 1989, *ApJ*, 345, 434
- Weatherall, J. C., 1998. *ApJ*, 506, 341
- Weisskopf, C. M. et al. 2000, *ApJ*, 536, L81

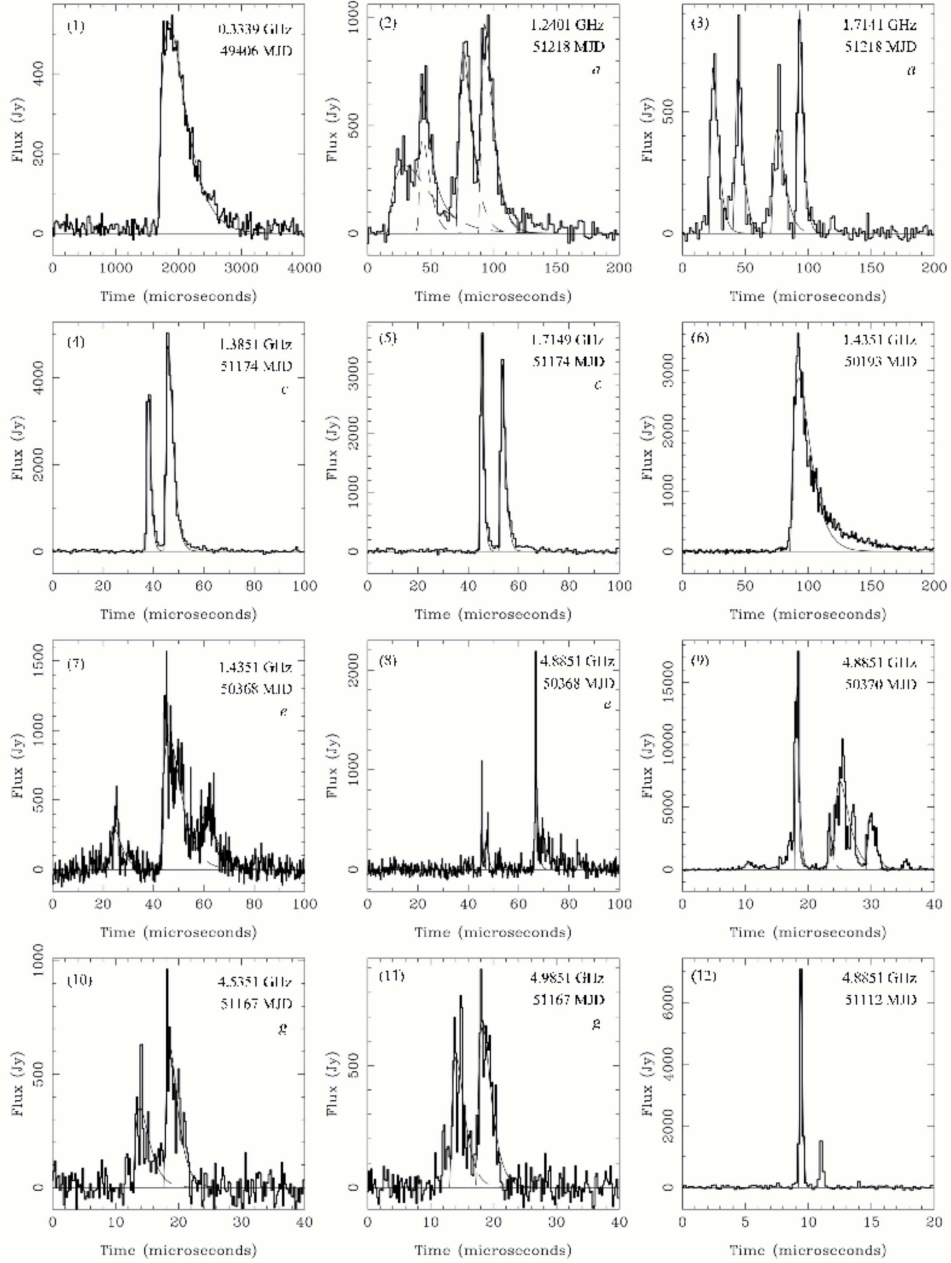


Fig. 1.— Examples of single pulses recorded from the Crab pulsar. These examples illustrate the fact that several microbursts are often seen in an individual pulse, except at 0.33 GHz where interstellar scattering dominates the profile. These examples also illustrate the gradual change of burst profiles from lower to higher frequencies. Each pulse is identified by center frequency and observing date (MJD), as well as a reference number at the top left. Pulses recorded simultaneously at two frequencies are identified by letters given below the observing dates; these letters correspond to superscripts in Table 1. Heavy lines show the data; light dashed lines are the functional fits to individual bursts, discussed in § 3; the light solid lines are their sum.

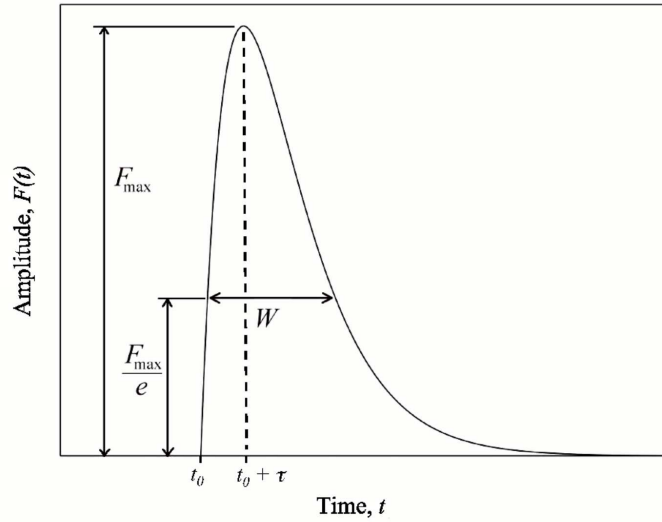


Fig. 2.— Illustration of the microburst fitting function, $F(t) = A(t - t_0)e^{-(t-t_0)/\tau}$. The function reaches a maximum, $F_{\max} = A\tau e^{-1}$, at a time $t = t_0 + \tau$. Its width, defined as $W = 3\tau$, is approximately the width at an amplitude of F_{\max}/e . The total fluence is $\mathcal{E} = \int F(t)dt = A\tau^2$.

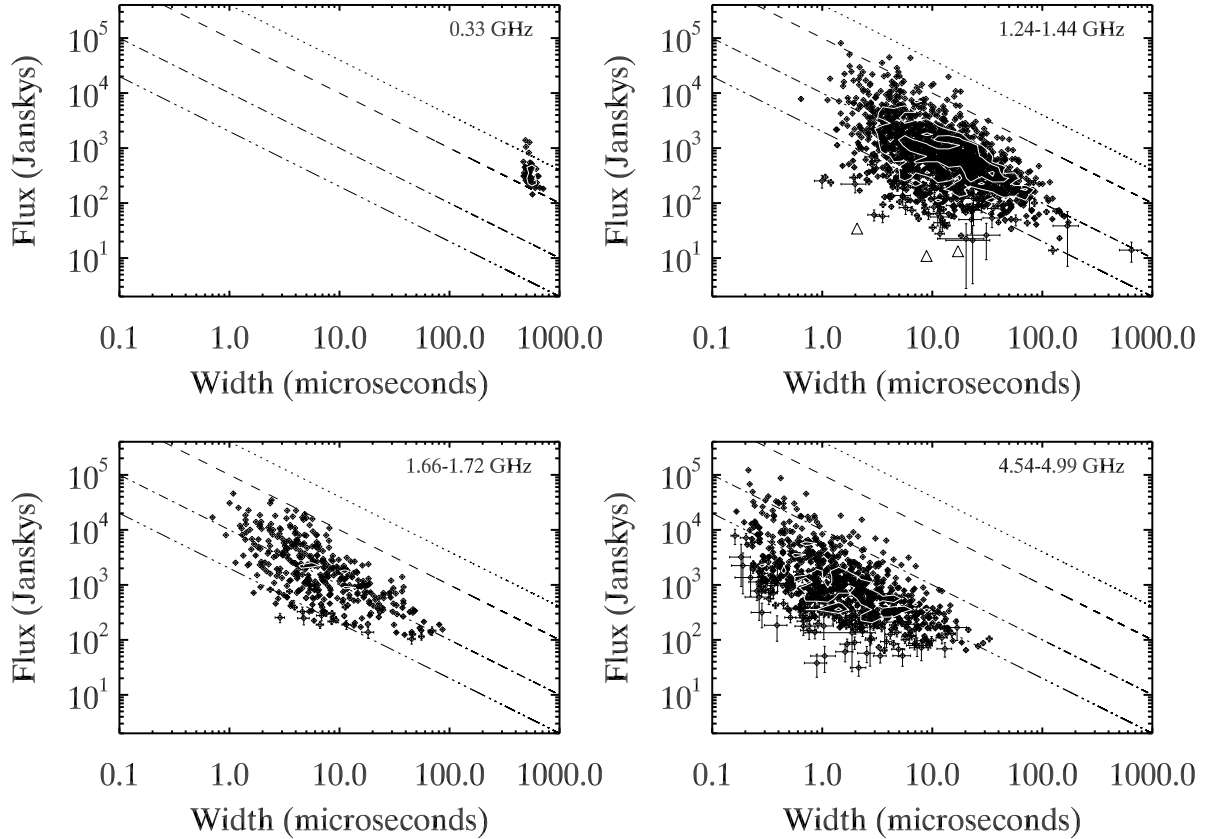


Fig. 3.— Distribution of the measured flux and width values for all observed microbursts, grouped by frequency as labeled. The overlaid lines show loci of constant fluence: dotted, 0.4 Jy-s; dashed, 0.1 Jy-s; dash-dot, 0.01 Jy-s; triple-dot-dash, 0.002 Jy-s. While bursts occupy a wide range of fluence, there is some tendency for brighter bursts to be short-lived, and fainter bursts to be longer-lived. The contours show point densities of 5, 10 and 20 points per bin; the bin size is 0.1 decade in log space.

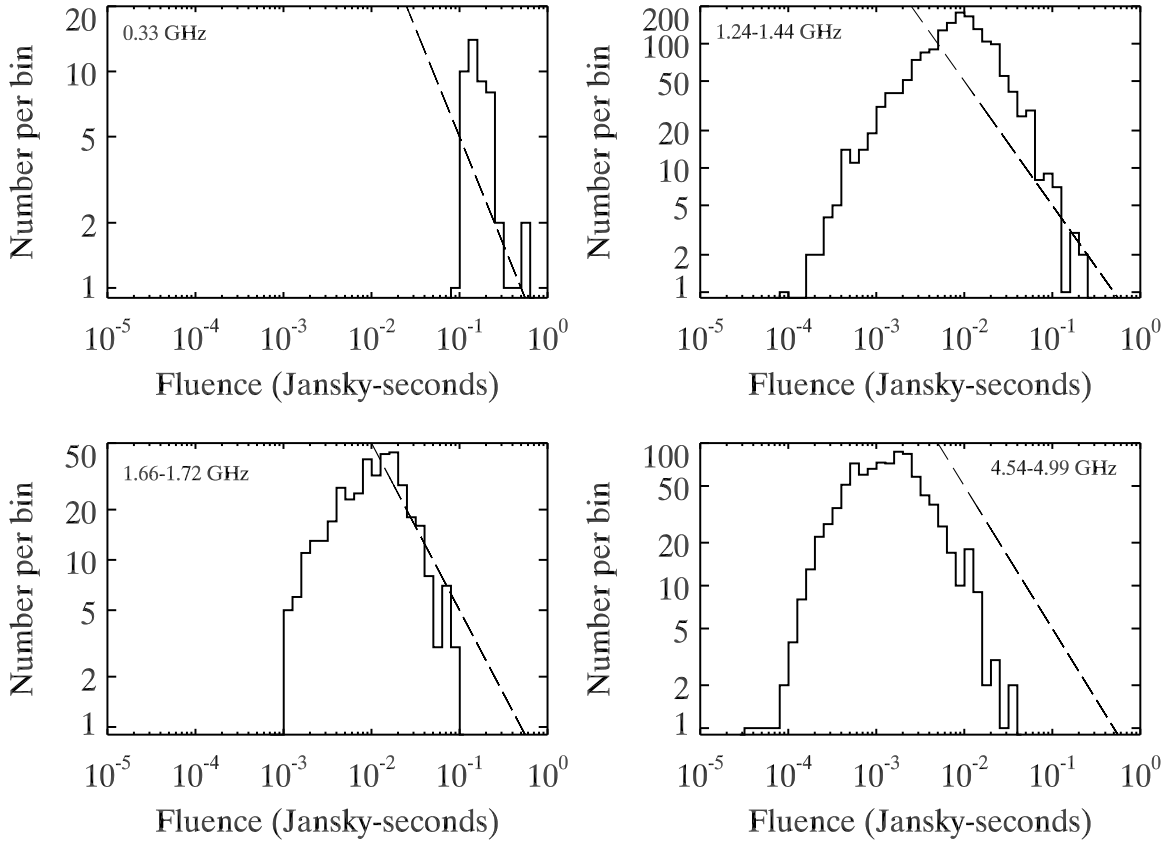


Fig. 4.— Distribution of fluences for all measured microbursts, displayed as a histogram in log space, grouped in the same frequency ranges used in Figure 3. The data in this figure are binned in one-tenth-decade intervals; the histogram values are not normalized to the bin size. Thus, the units of the vertical axis are “number of microbursts”, not “number of microbursts per fluence range”. The apparent low-fluence falloff is a result of incomplete sampling due to the triggering mechanism we used to record single pulses. The dashed line illustrates the \mathcal{E}^{-2} distribution which would result if all bursts release the same amount of energy which is modified only by relativistic beaming at different angles to the line of sight.

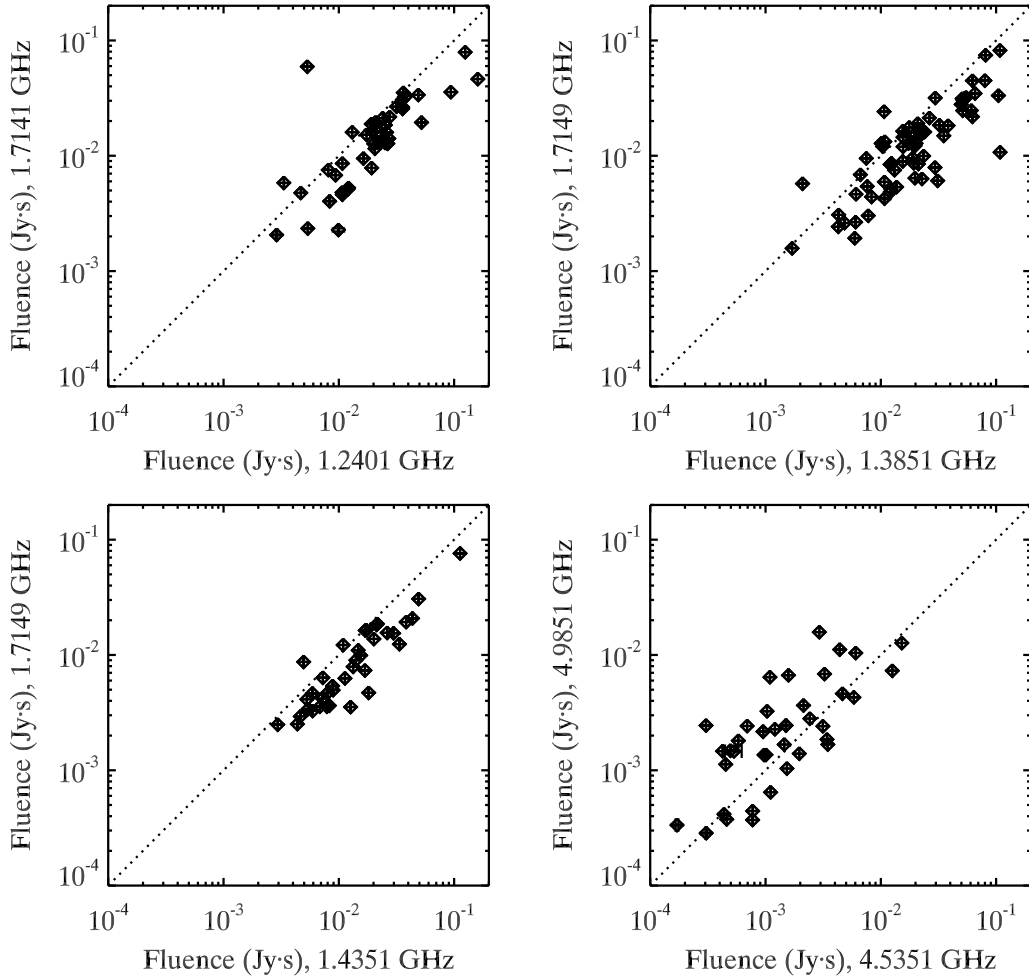


Fig. 5.— Fluences of individual microbursts measured simultaneously at two frequencies. The dotted lines show the location of high- and low-frequency fluence equality. Error bars determined during the burst fitting process are plotted for both axes; in all cases the error bars are as small or smaller than the plot symbol. The large scatter is physical, reflecting variation of burst-to-burst fluence. It is, nonetheless, apparent that bursts measured between 1 and 2 GHz tend to be stronger at the lower measured frequency.

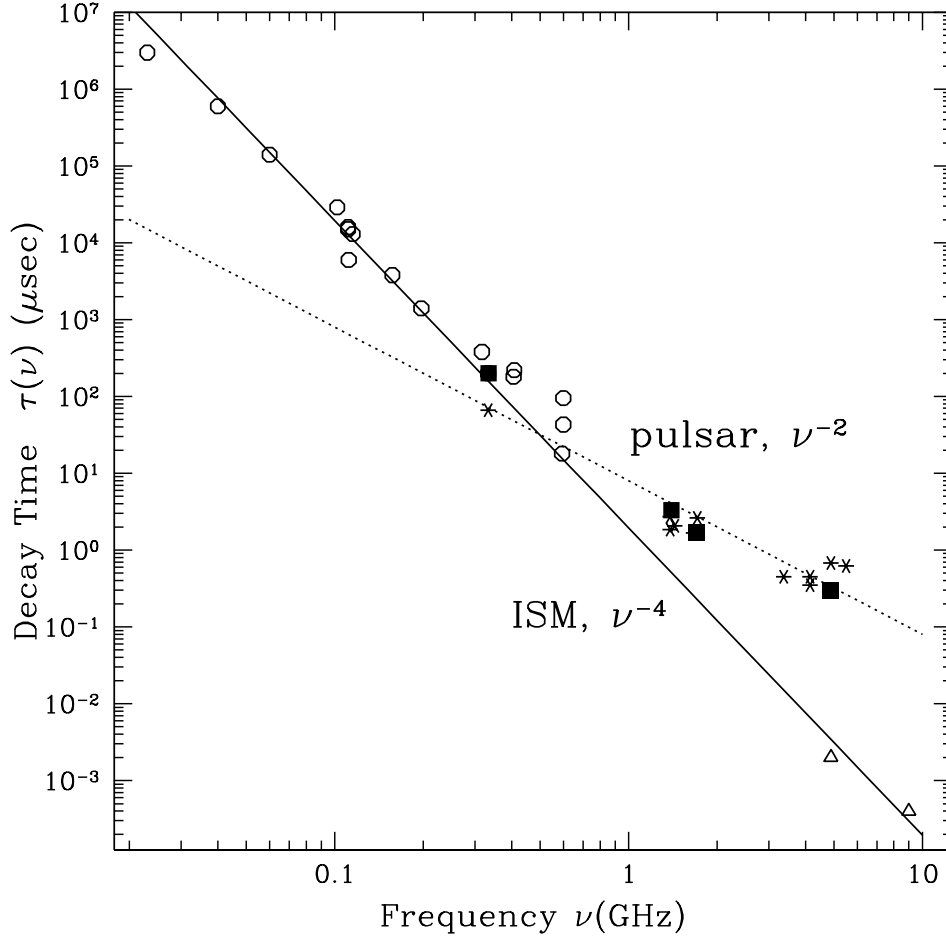


Fig. 6.— Pulse decay time as a function of frequency. Open circles show decay times from the literature, listed in Table 4. Filled squares are estimates of the “typical” microburst widths from our data, grouped by frequency as in Figure 3, and converted to decay times using $\tau = W/3$, as discussed in §5.4.2. Asterisks are decay times derived from mean fluctuation spectra, as listed in Table 5. Triangles show upper limits on nanoshot widths from Hankins et al. (2003), at 4.8 GHz, and Hankins & Eilek (2007), at 9 GHz. The solid line illustrates the $\tau(\nu) \propto \nu^{-4}$ behavior predicted by interstellar scattering on Gaussian turbulence. This line is not a formal fit to the points, but simply meant to illustrate the trend. The lower-frequency points from the literature (open circles), and the highest-frequency nanoshot points (triangles) appear consistent with the ISS line. However, the characteristic widths of our microbursts above 1 GHz (filled squares and asterisks) deviate dramatically from the ISS prediction. They are approximately consistent with a $\tau(\nu) \propto \nu^{-2}$ law, which we illustrate with a dotted line.

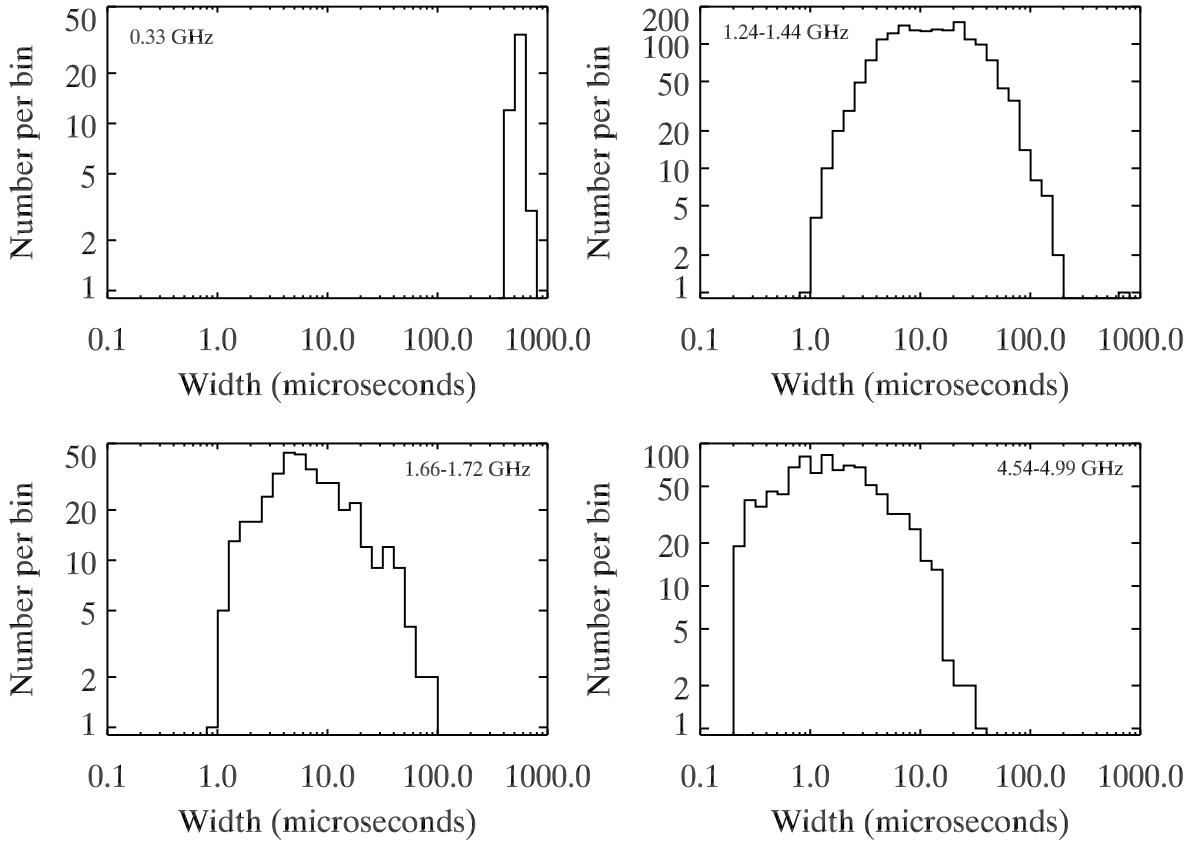


Fig. 7.— Distribution of widths for all measured microbursts, displayed as a histogram in log space, grouped in the same frequency ranges used in Figures 3 and 4. These data are binned in logarithmic intervals, as in Figure 4. At 0.33 GHz, the pulse widths are dominated by ISS. At higher frequencies, the broad width distribution is intrinsic to the pulsar, as discussed in §5.

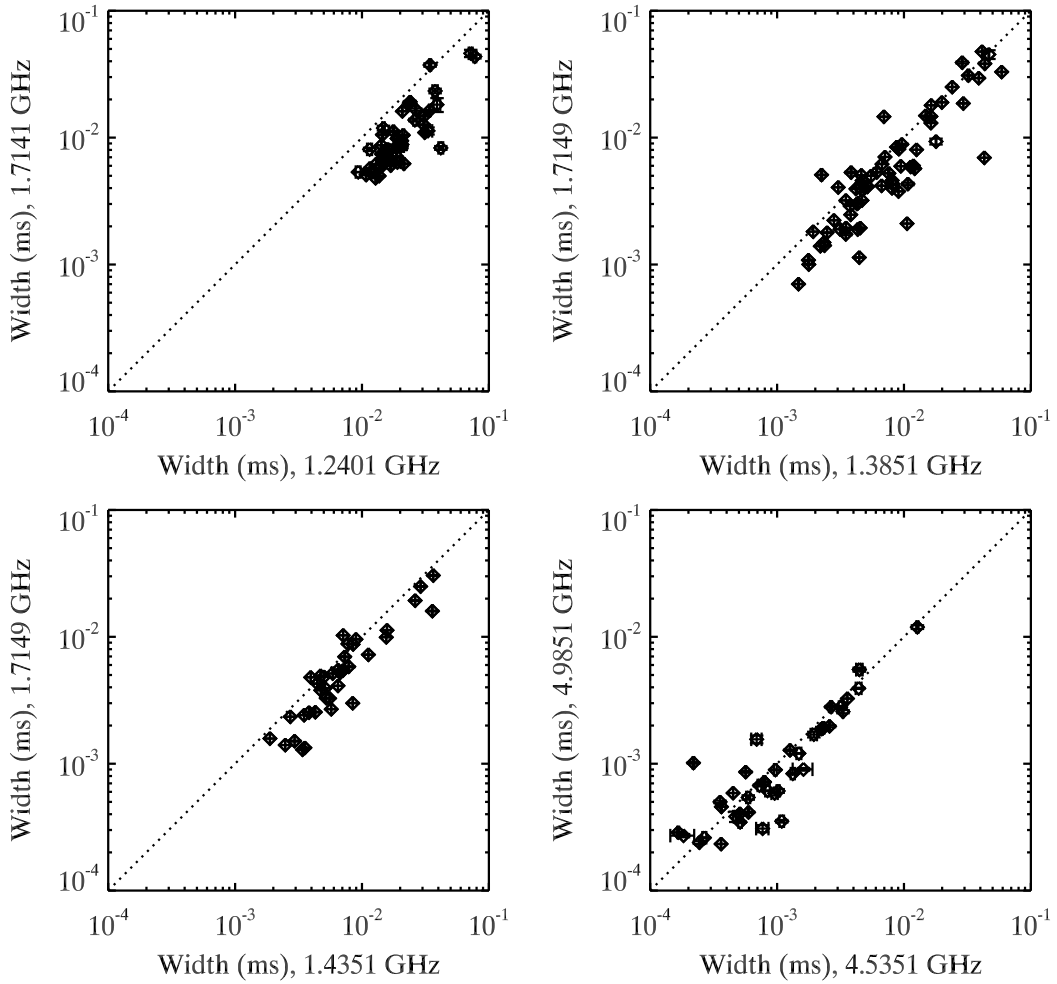


Fig. 8.— Widths of individual microbursts measured simultaneously at two frequencies. The dotted line shows the location of high- and low-frequency width equality. Error bars determined during the microburst fitting process are plotted for both axes; for most points the error bars are smaller than the plot symbols. The scatter is physical, reflecting burst-to-burst variation in widths. It is apparent that microbursts seen between 1 and 2 GHz tend to be broader when observed at the lower frequency.

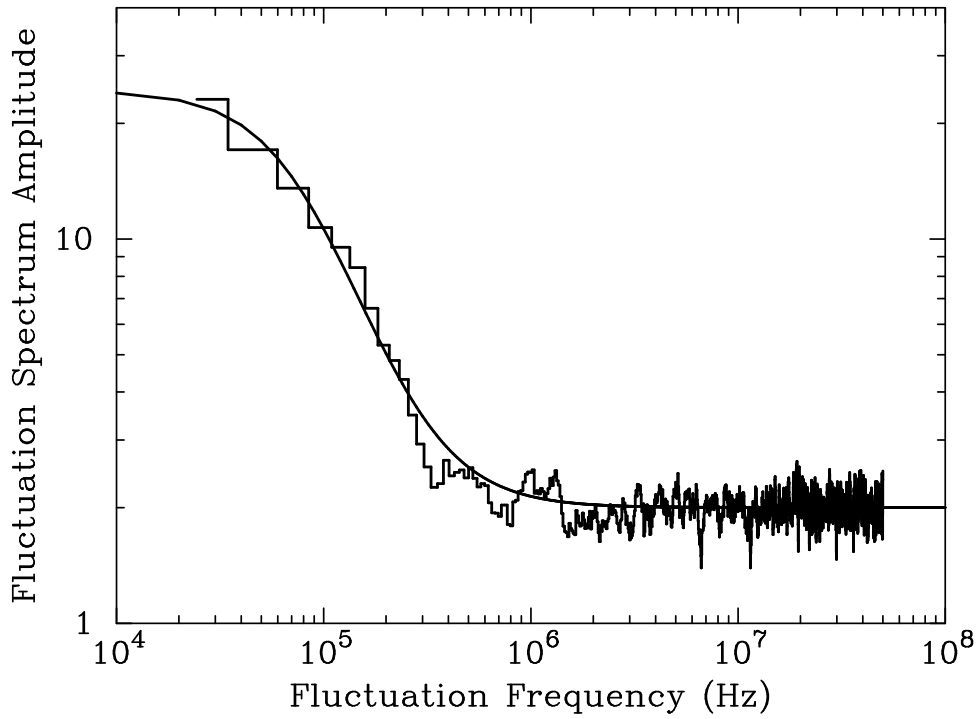


Fig. 9.— The mean, on-pulse fluctuation spectrum for a set of 34 pulses at 1.4351 GHz (MJD 50368). The solid line shows the best-fit estimate of the $n = 0$ template, $g_0(f)$, for which $\tau = 2.1 \mu\text{s}$. Because the fluctuation spectrum of each pulse was normalized before forming the mean, the vertical scale is arbitrary.

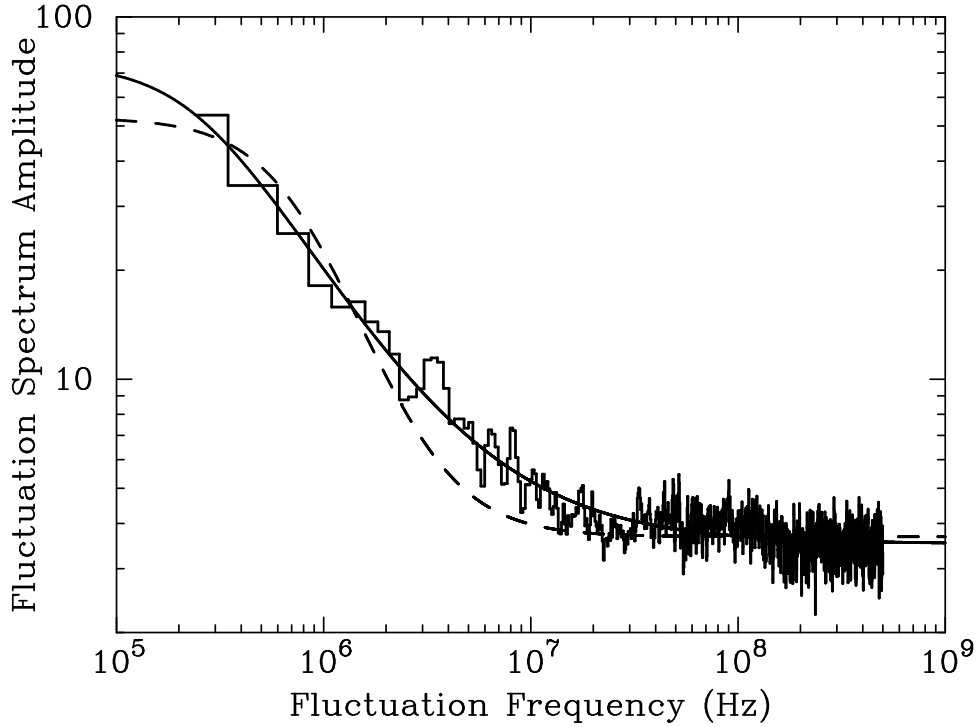


Fig. 10.— The on-pulse fluctuation spectrum for a set of 15 pulses at 5.5 GHz (MJD 52336). The solid line shows the best-fit estimate of the $n = -1/2$ template, $g_{-1/2}(f)$, for which $\tau = 0.62 \mu\text{s}$. The dotted line shows the best-fit $n = 0$ template, which clearly does not fit these data well. Other details are as in Figure 9; when compared with that figure the difference in the structure of the fluctuation spectrum is clear.

Table 1. VLA observations used for microburst analysis

Center Freq ¹ (GHz)	Band- width (GHz)	No. of pulses	No. of bursts	Smooth- ing time (μ s)	Time Span (min)	MJD
0.3339	0.003	49	49	20.0	18	49406
1.2401 ^a	0.025	38	61	1.6	55	51218
1.3851 ^b	0.500	27	52	0.8	41	51159
1.3851 ^c	0.500	52	97	0.8	20	51174
1.4149	0.500	61	142	0.8	26	49399
1.4351	0.500	52	95	0.8	14	51137
1.4351	0.500	50	131	0.8	11	51159
1.4351	0.500	54	123	0.8	15	51167
1.4351	0.500	51	119	0.8	10	51174
1.4351 ^d	0.500	34	81	0.8	13	51174
1.4351	0.500	51	81	0.8	22	51214
1.4351	0.500	203	259	0.8	59	50193
1.4351	0.500	103	200	0.8	84	50224
1.4351 ^e	0.500	34	69	0.8	30	50368
1.4351 ^f	0.500	61	108	0.8	170	50370
1.6649 ^b	0.500	70	145	0.8	41	51159
1.7141 ^a	0.025	38	63	1.6	55	51218
1.7149 ^c	0.500	52	101	0.8	20	51174
1.7149 ^d	0.500	34	74	0.8	13	51174
4.5351 ^g	0.500	46	96	0.2	41	51167
4.8851	0.500	51	104	0.2	57	49080
4.8851 ^e	0.500	40	79	0.2	31	50368
4.8851 ^f	0.500	62	117	0.2	170	50370
4.8851	0.500	34	54	0.2	16	51112
4.8851	0.500	152	312	0.2	126	51112
4.9851 ^g	0.500	52	145	0.2	42	51167

¹Superscript pairs denote simultaneous 2-frequency observing sessions.

Table 2. Arecibo observations used for fluctuation spectra

Center Freq (GHz)	Bandwidth (MHz)	number of pulses	MJD
3.375	250	16	52399
4.150	500	14	52334
4.150	500	12	52335
5.500	500	15	52336

Table 3. Fluence and width behavior of microbursts

Freq 1 (GHz)	Freq 2 (GHz)	No. of bursts	$\langle\alpha\rangle^a$	σ_α^a	$\langle\beta\rangle^b$	σ_β^b
1.2401	1.7141	46	-1.2	1.8	-2.2	0.9
1.3851	1.7149	68	-2.4	2.4	-1.6	2.1
1.4351	1.7149	37	-2.7	2.0	-1.8	1.8
4.5351	4.9851	41	4.8	8.2	-0.8	4.7

^aMean and standard deviation of fluence index, where $\mathcal{E}(\nu) \propto \nu^\alpha$.

^bMean and standard deviation of width index, where $W(\nu) \propto \nu^\beta$.

Table 4. Pulse scattering decay times below 1 GHz

Frequency (GHz)	Decay time τ (ms)	Reference
0.023	3000. ^a	Popov et al. (2006)
0.040	600. ^a	Kuzmin et al. (2002)
0.060	140. ^a	Kuzmin et al. (2002)
0.102	29. ^a	Kuzmin et al. (1996)
0.111	16. ^a	Kuzmin et al. (2002)
0.111	15. ^a	Popov et al. (2006)
0.112	6. ^a	Rankin et al. (1970)
0.115	13. ^a	Staelin & Sutton (1970)
0.157	3.8 ^a	Staelin & Sutton (1970)
0.197	1.4 ^a	Rankin et al. (1970)
0.317	0.38 ^a	Rankin et al. (1970)
0.333	0.20 ^b	this paper
0.408	0.22 ^a	Rankin et al. (1970)
0.406	0.18 ^a	Kuzmin et al. (2002)
0.594	0.018 ^a	Kuzmin et al. (2002)
0.600	0.095 ^b	Sallmen et al. (1999)
0.600	0.043 ^a	Popov et al. (2006)

^aEstimated from mean profile; Rankin’s values converted as $\tau = W/\sqrt{2}$.

^bEstimated from mean of individual profiles

Table 5. Characteristic decay times from fluctuation spectra

Frequency (GHz)	Decay time τ_{char} (μs)	Observ- atory	MJD
0.3330	^a 66.0	VLA	49406
1.3851	^a 2.72	VLA	51159
1.3851	^a 1.85	VLA	51174
1.4351	^a 2.07	VLA	50368
1.6649	^a 1.67	VLA	51159
1.7149	^b 2.63	VLA	51174
3.3750	^b 0.45	AO	52399
4.1500	^b 0.35	AO	52334
4.1500	^b 0.45	AO	52335
4.8851	^b 0.68	VLA	50368
5.5000	^b 0.62	AO	52336

^aDecay time determined using $n = 0$ case

^bDecay time determined using $n = -1/2$ case